Closing the Loop on Concentric Tube Robot Design: A Case Study on Micro-Laryngeal Surgery

Jui-Te Lin, Cédric Girerd, Benjamin T. Ostrander, Parsa Molaei, *Member, IEEE*, Hunter B. Gilbert, *Member, IEEE*, Philip A. Weissbrod, John T. Hwang, and Tania K. Morimoto, *Senior Member, IEEE*

***Abstract*—Concentric tube robots (CTRs) are well-suited to address the unique challenges of minimally invasive surgical procedures due to their small size and ability to navigate highly constrained environments. However, uncertainties in the manufacturing process can lead to challenges in the transition from simulated designs to physical robots. In this work, we propose an end-to-end design workflow for CTRs that considers the often-overlooked impact of manufacturing uncertainty, focusing on two primary sources — tube curvature and diameter. This comprehensive approach incorporates a two-step design optimization and an uncertainty-based selection of manufacturing tolerances. Simulation results highlight the substantial influence of manufacturing uncertainties, particularly tube curvature, on the physical robot's performance. By integrating these uncertainties into the design process, we can effectively bridge the gap between simulation and real-world performance. Two hardware experiments validate the proposed CTR design workflow. The first experiment confirms that the performance of the physical robot lies within the simulated probability distribution from the optimization, while the second experiment demonstrates the feasibility of the overall system for use in micro-laryngeal surgical tasks. This work not only contributes to a more comprehensive understanding of CTR design by addressing manufacturing uncertainties, but also creates a new framework for robust design, as illustrated in the context of micro-laryngeal surgery.**

***Index Terms*—Medical robots and systems, surgical robotics, concentric tube robots, multidisplinary design optimization, micro-laryngeal surgery.**

Manuscript received 10 May 2024; accepted 1 July 2024. Date of publication 2 September 2024; date of current version 22 November 2024. This work was supported by National Science Foundation under Grant 2146095. *(Corresponding author: Jui-Te Lin.)*

Jui-Te Lin is with the Department of Mechanical and Aerospace Engineering, University of California, San Diego, La Jolla, CA 92093 USA (e-mail: jul024@eng.ucsd.edu).

Cédric Girerd is with the LIRMM, Univ Montpellier, CNRS, France.

Benjamin T. Ostrander and Philip A. Weissbrod are with the Department of Otolaryngology - Head & Neck Surgery, University of California, USA.

Parsa Molaei and Hunter B. Gilbert are with the Department of Mechanical and Industrial Engineering, Louisiana State University, USA.

John T. Hwang is with the Department of Mechanical and Aerospace Engineering, University of California, USA.

Tania K. Morimoto is with the Department of Mechanical and Aerospace Engineering and the Department of Surgery, University of California, USA.

Digital Object Identifier 10.1109/TBME.2024.3426489

I. Introduction

CONTINUUM robots have significant potential for impact in surgical applications, due to their ability to safely traverse constrained environments and perform dexterous manipulation tasks [1]. Compared to traditional rigid serial manipulators, the design of continuum robots is particularly challenging due to the large design space and non-intuitive kinematics. In addition, the design of these robots can often depend on the specific medical intervention and the patient's anatomy [2]. There has therefore been significant work on the development of design optimization tools for these robots in order to ensure they can meet the requirements for a given application. However, the outcomes of these design optimizations are frequently not evaluated or verified with physical prototypes, which can vary significantly from the simulated design due to uncertainties in the fabrication process. In this work, we propose an end-to-end design framework for one type of continuum robot, known as a concentric tube robot (CTR), that accounts for the manufacturing uncertainty during the design process. We then demonstrate the use of this framework through a case study focused on micro-laryngeal surgery using the proposed dual-CTR system, shown in Fig. 1.

A. Concentric Tube Robot Design

Concentric tube robots (CTRs) [3], [4] consist of multiple concentrically-assembled, superelastic tubes. Each tube typically consists of two sections — a straight section at the proximal end and a pre-curved section at the distal end. The shape of the robot can be actively controlled by relative translation and rotation of the tubes with respect to each other. With a diameter range of 1 mm to 3 mm, CTRs are particularly well-suited for clinical applications that require manipulation in highly constrained environments. In order to optimize the design of CTRs, both gradient-based and gradient-free approaches have been proposed. Gradient-free solvers can locate the global minimum by exploring the design space, but often demand a higher

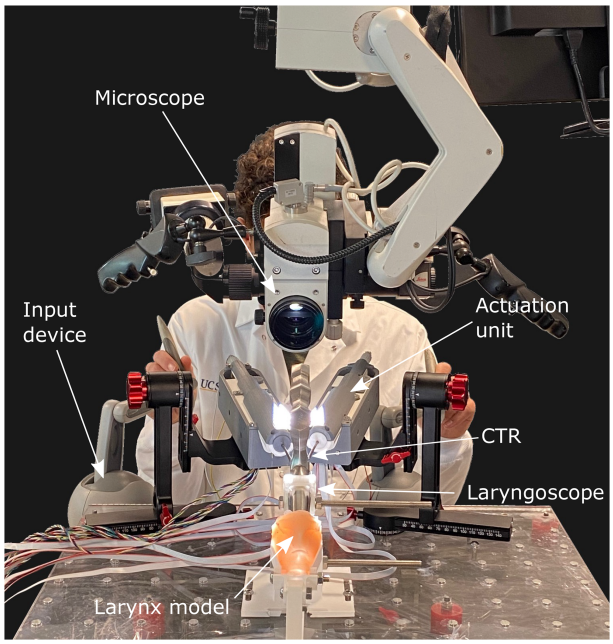

Fig. 1. Proposed dual-CTR system for micro-laryngeal surgery. This system uses a microscope to visualize the larynx through a laryngoscope and the CTRs are teleoperated using two 6-DOF input devices.

number of iterations and therefore computation time [5]. In contrast, gradient-based methods scale linearly or better as the number of design variables increases [5], making them well-suited for solving large-scale optimization problems. However, gradient-based solvers require both the model and the function to be continuous and differentiable to fully harness the benefits of gradient descent, and challenges arise when the objective or constraints are non-continuous, which is the case for most of the CTR design optimization problems.

The majority of CTR design optimizations to date have focused on workspace coverage and reachability as the primary objectives [6], [7]. These objectives are computationally intensive problems, which are further exacerbated by the complexity of the kinematic model and the vast design space. Leibrandt et al. recently proposed a new global metric to evaluate reachability and dexterity efficiently using a voxelisation approach suitable for design optimization problems [8]. Another metric, which has received limited attention despite its importance for many applications, is orientability. Orientability, as a metric, quantifies the number of robot configurations capable of reaching the target. It is important to note that a redundant robot possesses an infinite number of orientations for a given tip position, in contrast to the single orientation available to a non-redundant robot [9]. A high orientability in the CTR indicates that the robot can reach the target from a large range of orientations [10]. This allows for greater manipulation of tissue from different angles. Incorporating orientability into the optimization framework is particularly challenging, as it significantly increases the scale of the optimization and motion planning problem owing to the infinite number of orientations that can be reached in the workspace. Additionally, there is no analytical form that can describe the orientability problem, unlike the dexterity index, which can be derived from the condition number of the Jacobian matrix. Therefore, most related work on the orientability problem has focused on analyzing the orientability of existing robot designs, rather than integrating it into CTR design optimization framework. In this work, we integrate the orientability problem into CTR design optimization by proposing a new orientability metric.

B. Challenges in CTR Manufacturing

CTRs are most commonly made by shape setting Nitinol tubes. Although it is possible to obtain custom, shape-set tubes directly from the tube suppliers, this approach is very expensive, and can still be subject to manufacturing uncertainties. Therefore, researchers have proposed several methods for the fabrication of CTR tubes. The most common approach is to heat-set the Nitinol tubes in a furnace using a custom fixture with the desired curvature. The tubes are typically heated in a temperature range of $500 - 550°$ for $10 - 20$ minutes, depending on manufacturer recommendations, as well as the type and size of the furnace used [11]. The furnace approach often requires significant experimentation and can result in large spring-back after release from the fixture. Gilbert et al. developed an electric shape-setting system that increases the temperature of a tube using the Joule effect [12]. This approach offers the benefit of more rapid prototyping and a greater reduction in spring-back compared to the furnace method. However, optimized tube curvatures may still not be perfectly obtained and some tuning of the temperature and fixture curvature may be needed. Depending on the number of iterations required for both the furnace and Joule-heating methods, the overall cost, in terms of materials and labor, can increase substantially. In general, reducing manufacturing tolerances typically leads to increased costs, which can rise either linearly or exponentially depending on the manufacturing method employed [13]. Therefore, similar to many engineering design problems, it is important to find an appropriate balance between cost, accuracy, and manufacturability.

C. Micro-Laryngeal Surgery

Micro-laryngeal surgery is a minimally invasive endoscopic procedure for treating a variety of conditions in the larynx, pharynx, and hypopharynx. The procedure is typically accomplished using a variety of long, rigid instruments passed transorally through a laryngoscope. However, the curvilinear path between the oral opening and surgical target can pose a significant challenge for visualization and manipulation using the rigid instruments. In addition to access issues, micro-laryngeal surgery can be a very technically difficult procedure, subject to anatomical and ergonomic constraints, restrictions in range of motion, hand tremors, and fatigue, all of which can contribute to unsatisfactory surgical outcomes [14]. Another approach has been to use robotic technology to perform these challenging head and neck procedures. One state-of-the-art robotic system, the da Vinci robot from Intuitive Surgical (Sunnyvale, California, USA), has been applied to transoral surgery to gain access to these regions. However, the instrument size and limitations in their maneuverability make it difficult to operate in the narrow

confines of the larynx [15]. MedRobotics (Raynham, USA) developed a robotic system specific for micro-laryngeal surgery that used a flexible continuum robot to carry a camera and two instruments through the curvilinear path to the larynx. However, the device is no longer on the market and had a number of limitations, including the instrument size [16]. Finally, Friedrich et al. demonstrated the feasibility of using a teleoperated single-arm continuum robot to navigate and reach surgical targets in a porcine larynx model [17].

D. Contributions

The contributions of this work are as follows. (1) We propose a comprehensive end-to-end design workflow for CTRs that accounts for manufacturing uncertainty. The approach considers the uncertainty of tube curvature during the shape-setting process and provides fabrication tolerances that aim to balance the cost and the robot performance. The design process incorporates an improved rapid, low-cost electric shape-setting method. (2) We present a formulation for incorporating the orientability into the objective function for gradient-based CTR design optimization for the first time. In addition, we introduce a new orientability representation and use it to compute the orientability of the optimized design. (3) We present the first study using a dual-CTR system designed specifically for applications in micro-laryngeal surgery. We first show that the orientability of both physical robots are within the expected performance distribution after the manufacturing process. We then conduct a user test to validate the feasibility of the proposed system and surgical workflow for performing a biopsy task using a phantom model.

II. CTR Design Optimization

In this section, we propose a gradient-based optimization method with the goal of maximizing the orientability inside the surgical workspace. Our approach incorporates both reachability and orientability objectives in the optimization problem, which we present in the context of micro-laryngeal surgery.

A. Task-Specific Design Requirements

1) Line of Sight: Maintaining a line of sight to the surgical target is necessary for current micro-laryngeal surgical setups, since a microscope is used to provide visualization through a laryngoscope. In this work, we try to maintain the standard surgical workflow and setup as much as possible in order to lower the barrier for adoption. Therefore, in order to meet the line-of-sight requirement and to fit two CTRs within the laryngoscope-microscope configuration, the actuation system for the proposed dual-CTR is designed with a Y-shape [18], [19], rather than with two parallel actuation units. We select an angle of 45° between the two CTR actuation units to ensure that they do not block the surgeon's view, as shown in Fig. 2. The surgical workspace is typically inside the boundary of the laryngoscope at its distal end. We define the workspace here as a $6\text{ mm} \times 6\text{ mm} \times 6\text{ mm}$ cube, based on feedback from clinicians at the University of California San Diego. Six surgical targets were selected at the center of each face of the cube, as visible in Fig. 2.

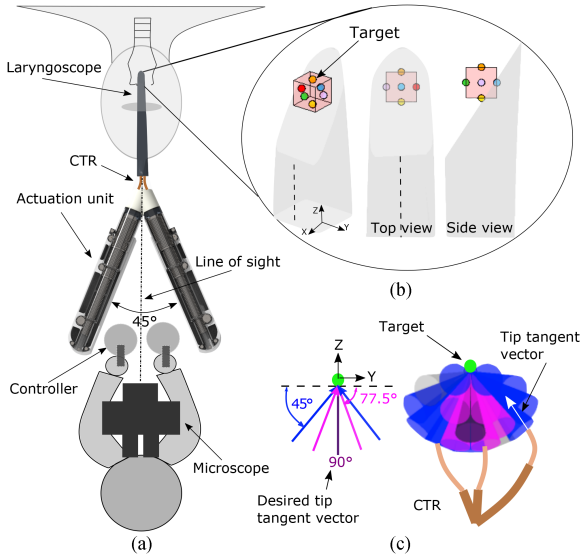

Fig. 2. (a) Schematic showing the proposed micro-laryngeal CTR system, which aims to maintain the standard clinical workflow. (b) Surgical workspace and targets at the distal end of the laryngoscope as identified based on feedback from clinicians. (c) Three distinct angles (45° (blue), 77.5° (pink), and 90° (purple)) are represented as vectors in 2D (Y-Z plane). These vectors can then be used to construct 3D cones when rotating them about the z-axis.

2) Orientability: Traditional micro-laryngeal surgery involves the use of multiple long, rigid instruments with pre-angled distal ends. Surgeons often switch between instruments to maintain line of sight and improve ergonomics when performing various tasks in different locations in the larynx, which requires different angles with the tissue. The goal of the design optimization is to maximize the orientability in the targeted workspace. To incorporate orientability into a gradient-based optimization problem, it must be formulated in a way that is continuous and differentiable. Unlike sampling-based methods that explore the entire joint space to obtain tip orientations, our approach discretizes orientations into a finite set of target orientations. The target orientations are defined as 3D vectors. The optimizer seeks to minimize the norm of the vector difference between the target and the tangent vector of the robot tip. We generate a cone-like shape for each orientation, where the boundary of each cone is based on a defined tolerance. This concept is illustrated in Fig. 2(c). Orientations required for typical micro-laryngeal surgical tasks are identified by clinicians to be in the range between $45^\circ - 90^\circ$ based on the existing surgical tools. To obtain the desired vectors $\mathbf{t_{des}}$ for the CTR tip tangent vector to reach, we select three discrete orientations (45°, 77.5°, and 90°) within the range and rotate these vectors about the z-axis, as shown in Fig. 2(c). Orientations are discretized into 19 total different target vectors (12 vectors for 45°, 6 vectors for 77.5° and 1 for 90°) based on a 10° tolerance, which is chosen in order to minimize the empty space between each cone. Then, the set of cones can be readily derived and positioned around each predefined target.

B. Problem Formulation

We propose to simplify the dual-CTR optimization problem by leveraging the symmetric nature of the laryngoscope. We

divide the laryngoscope into a right and a left workspace, as illustrated by the dashed line in Fig. 2, and instead optimize just a single CTR design to remain within the boundary of just one of these workspaces. By doing so, we aim to reduce the risk that the two robot backbones collide with each other. We note that the opening at the distal end of the laryngoscope remains the same, without dividing it into two, since the two CTRs will need to interact for collaboration tasks. For the optimization, the robot is placed on the left side of the laryngoscope from the top view (see Fig. 2(b)).

The optimization problem formulation is based on our previous work [20]. Here, the goal is to obtain a robot design, $\mathbf{d}$, that maximizes the orientability of the CTR while avoiding collisions with the given half of the laryngoscope workspace. Each CTR is composed of four super-elastic pre-curved tubes, with a fixed base frame that is predefined based on geometric constraints. The overall design space includes the tube design parameters and joint variables of the robots. The robot design vector $\mathbf{d} \in \mathbb{R}^{5n}$ includes the tube curvature (κ_i), length of the straight section (L_{s_i}), length of the curved section (L_{c_i}), inner diameter (ID_i), and outer diameter (OD_i) of tube i. The joint vector $\mathbf{q} \in \mathbb{R}^{2n}$ consists of the tube rotation α_i at the base and tube translation β_i with respect to $s = 0$, where s is the arc length along the entire robot, i is the tube number where $i = 1$ the innermost tube to n, the outermost tube. Note that the outer-most tube, which serves as a guide, does not have any degrees of freedom, which is equivalent to having constant joint values. In this study, this tube guide was made of Nitinol, the same material as the other tubes. However, other materials, such as stainless steel for example, can also be used. In summary, the optimization problem is to find an optimized robot design $\mathbf{d}^*$ and a set of joint values $\mathbf{q}^*$ such that the robot can avoid collisions with the laryngoscope while reaching the predefined targets, $\mathbf{p_{des}}$, and orientations, $\mathbf{t_{des}}$, as previously described. Therefore, the overall CTR design space D can be described as:

$$D = \{\mathbf{d} \in \mathbb{R}^{5n}, \mathbf{q} \in \mathbb{R}^{2(n-1)\times m\times o}\}, \tag{1}$$

where n is the number of tubes, m is the number of targets, and o is the number of orientations.

C. Optimization Approach

The CTR orientability problem is a large-scale design optimization problem due to the combination of tube design parameters and joint values that need to be considered and optimized simultaneously. Therefore, in this work, we build on our previously proposed gradient-based CTR design optimization framework, which we showed to be scalable and efficient [20]. The optimizer SNOPT is used to solve the nonlinear programming problem and find solutions that are locally optimal. The framework solves an initial value problem, which is formulated as a set of differential equations that describes the tube angle ψ_i and tube torsion $\dot{\psi}_i$ along the backbone of the robot [21]:

$$\ddot{\psi}_i = \frac{k_{ib}}{k_{it}k_b}\sum_{j=1}^{n} k_{jb}\kappa_i\kappa_j \sin(\psi_i - \psi_j), \tag{2}$$

where κ_i is the curvature, k_{ib} the bending stiffness, k_{it} the torsional stiffness of tube i, and $k_b = \sum_{i=1}^{n} k_i$, and the overdot refers to derivatives with respect to the curvilinear abscissa s along the robot. The torsion of tube i at the distal end ($s = L_i + \beta_i$) is zero since it is a free end. The other initial conditions are the tube angles at the tip, which are treated as the optimization variables in [20]. Therefore, the initial conditions can be written as follows [22]:

$$\begin{aligned} \psi_i(L_i + \beta_i) &= \phi_i \\ \dot{\psi}_i(L_i + \beta_i) &= 0. \end{aligned} \tag{3}$$

After solving for the tube angle along the backbone, the resultant curvature vector can be derived as follows [21]:

$$\mathbf{u} = \mathbf{K}^{-1}\sum_{i=1}^{n}\mathbf{K}_i(\mathbf{R}_{\psi_i}\mathbf{u}_i^* - \dot{\psi}_i\mathbf{e}_3), \tag{4}$$

where $\mathbf{K_i}$ is the stiffness matrix of tube i, $\mathbf{K} = \sum_{i=1}^{n} K_i$, $\mathbf{u_i^*}$ is the precurvature vector of tube i, and $\mathbf{e_3}$ is the standard unit vector along the z-axis. In order to reconstruct the 3D points and orientations along the robot backbone, the shape of the innermost tube, which crosses the entire robot, can be obtained to compute the robot shape. For this, two additional first-order differential equations need to be solved and can be written as [21]:

$$\begin{aligned} \dot{\mathbf{R}} &= \mathbf{R}\hat{\mathbf{u}}, \quad \text{with} \quad \mathbf{R}(0) = \mathbf{R}_z(\psi_1(0)) \\ \dot{\mathbf{p}} &= \mathbf{R}\mathbf{e}_3, \quad \text{with} \quad \mathbf{p}(0) = \begin{bmatrix} 0 & 0 & 0 \end{bmatrix}^T \end{aligned} \tag{5}$$

where the initial condition $\mathbf{R}(0)$ is the rotation about the z-axis by $\psi_1(0)$, and $\mathbf{p}(0)$ is the position of robot base, considered to be at the origin $s = 0$. The kinematics model is integrated into the optimization framework in order to maximize the reachability and orientability of the CTR by solving the inverse kinematics problem.

The goal of the optimization problem is to find a robot design such that the robot can have a collision-free deployment to reach all the targets with all possible orientations. All objectives must be continuous and differentiable for the gradient-based optimizer. The objective function used in [20] is used here, along with an additional term for orientability. The modified objective function is given by (6):

$$\begin{aligned} f(x) = {} & \underbrace{\zeta\sum_{i=1}^{a}\left(\sum_{j=1}^{v} dc_{i,j}(x)^{0.125}P_{i,j}(x)\right)}_{f_1(x)} \\ & + \underbrace{\epsilon_e\frac{\sum_{i=1}^{a-1} dp_i^2(x)}{\left(\sum_{i=1}^{a-1} dp_0(x)\right)^2}}_{f_2(x)} + \underbrace{\frac{\rho}{2}\left(\frac{||\mathbf{p}_{tip} - \mathbf{p}_{des}||_2}{||\mathbf{p}_0||_2}\right)^2}_{f_3(x)} \\ & + \underbrace{\lambda\frac{||\mathbf{p}_{tip} - \mathbf{p}_{des}||_2}{||\mathbf{p}_0||_2}}_{f_4(x)} + \underbrace{\epsilon_o||\mathbf{t_{tip}} - \mathbf{t_{des}}||_2}_{f_5(x)}, \end{aligned} \tag{6}$$

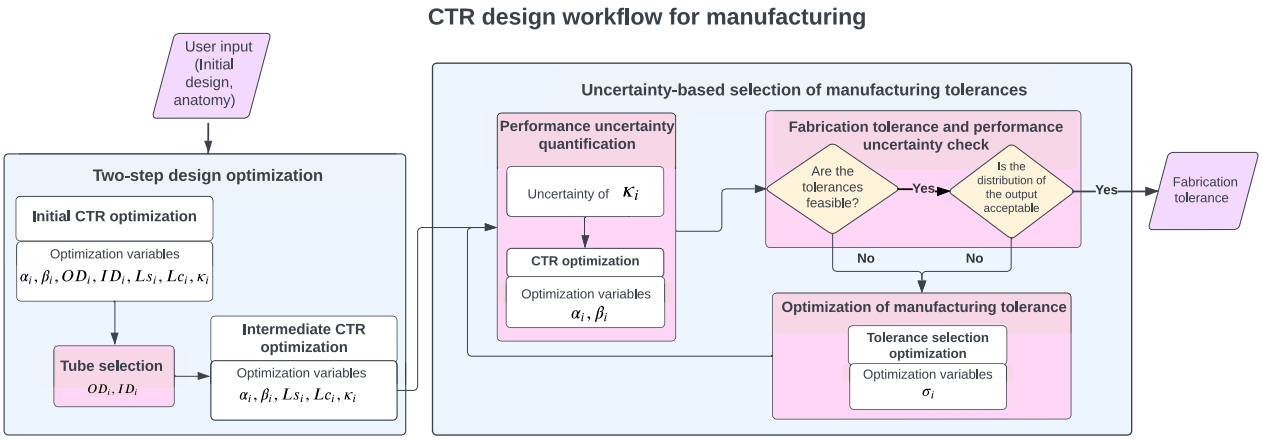

Fig. 3. Illustration of the proposed CTR design workflow for manufacturing. The workflow consists of two main parts. The first block is the two-step design optimization where two design optimization processes are performed in order to finalize the tube design for shape setting. The next block aims to determine the fabrication tolerance for tube curvature, κ_i, through an uncertainty-based selection of manufacturing tolerances.

where f_1 accounts for the collision avoidance using the distance $dc_{i,j}$ between the backbone points and the point cloud of the laryngoscope and the signed function, $P_{i,j}$. a is the number of backbone points, v is the number of points in the point cloud of the laryngoscope, and ζ is the weight. f_2 prevents the optimizer from favoring the deployment of the inner-most tube by penalizing the difference dp_i between the tube deployed lengths, and ϵ_e is a scaling factor. f_3 and f_4 are the formulations of the augmented Lagrangian method addressing the tip position error, where $\mathbf{p_{tip}}$ is the tip position, $\mathbf{p_{des}}$ is the desired tip position, ρ is a scaling term, and λ is the Lagrange multiplier. More detailed explanations can be found in [20]. Lastly, the new term f_5 is a task-specific objective to minimize the error between the tangent vector at the robot tip, $\mathbf{t_{tip}}$, and the desired vector, $\mathbf{t_{des}}$, where ϵ_o is a scaling factor. The penalty method is used for this term to simplify the tuning process. We note that as a consequence of the snapping problem for CTRs, the feasibility of a task-space trajectory between reachable points is not guaranteed. In this work, we perform the stability analysis proposed in [23] after the optimization to ensure that the tube set is stable. In scenarios where the optimized tube set is not stable across the workspace, one may proceed with the tube set if the unstable region does not overlap with the task space. Alternatively, a control algorithm can be implemented to avoid the unstable configurations. However, if task-critical desired configurations are unstable, the tube set should be re-optimized by adjusting the initial conditions or constraints. Future work may include the stability constraint in the optimization problem.

III. CTR Design Workflow for Manufacturing

During the CTR design and fabrication process, various sources of error are inherent and difficult to eliminate completely. The fabricated tube design and motion plan may therefore deviate from the optimized ones. However, there have not been significant efforts to investigate techniques for ensuring that the optimized tube design remains close to optimal in the presence of fabrication errors, or for ensuring that the performance of the physical robot still meets the design optimization goal. Although there are several other potential sources of uncertainty that could contribute to the gap between simulation and physical prototype, including uncertainties in mechanical properties (e.g flexural stiffness) and unmodeled phenomena (e.g tube clearance and friction), in this work, we focus on addressing a dominant factor—manufacturing uncertainty. The two primary sources of manufacturing uncertainty between the planned design and the fabricated prototype are differences between the optimized tube diameters and the sizes of tubes supplied by vendors, and the discrepancy in tube curvature resulting from spring-back after shape setting [12]. In order to address these issues, we propose a methodology, as shown in Fig. 3 and Algorithm 1, to bridge the gap between the design optimization and the physical robot under manufacturing uncertainties.

Importantly, this approach strives to balance robot performance with fabrication tolerance, directly impacting manufacturing costs.

A. Two-Step Design Optimization

The proposed two-step design optimization workflow is illustrated in Fig. 3. The predefined parameters are as follows: the number of tubes is $n = 4$, the number of targets is $m = 6$, and the number of orientations, denoted as o, is set to 10 for targets 1 to 5 and 18 for target 6. Compared to all orientations being considered for target 6, targets 1 to 5 only consider half of the orientations. This is because the laryngoscope is split in two, and the robot backbone might collide with the center line in order to reach the orientations from the other side, as illustrated in Fig. 4(a). An initial CTR optimization is performed based on the problem formulation in Section II-B, where all the optimization variables are considered. This optimized design is then used to select tubes from available suppliers (EUROFLEX GmbH in this case). Due to the high cost of custom Nitinol tubes, off-the-shelf tubes with diameters as close to the optimized diameters as possible are selected. To ensure that the objective can still be met, the tube design is then re-optimized in an intermediate

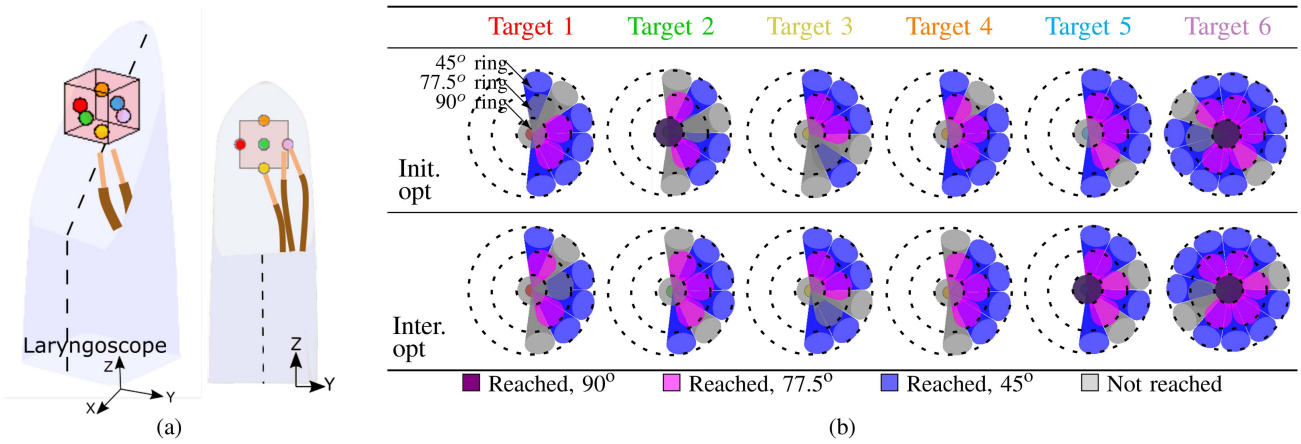

Fig. 4. Results of the two-step design optimization. The initial and intermediate CTR optimization results are presented, with reachable orientations depicted in color and unreachable orientations in gray. Six predefined targets, labeled 1 to 6, are marked in distinct colors, corresponding to their positions in the illustration on the left that indicates their locations relative to the robot and the laryngoscope. The total orientability is 78% and 72% for the initial and intermediate optimizations, respectively.

TABLE I
OPTIMIZED TUBE DESIGN VARIABLES

Opt. step	Variable	Optimized values			
		Tube 1	Tube 2	Tube 3	Tube 4
Initial	ID (mm)	0.65	1.51	2.02	2.73
	OD (mm)	1.36	1.86	2.64	3.22
	L_s (mm)	230.00	189.93	59.60	35.63
	L_c (mm)	10.14	20.06	50.43	29.56
	κ (mm^{-1})	0.0220	0.0081	0.0029	0.0178
Intermediate	ID (mm)	0.85*	1.47*	2.19*	2.7*
	OD (mm)	1.32*	2.03*	2.55*	3.0*
	L_s (mm)	230.01	190.00	60.00	35.02
	L_c (mm)	9.99	19.99	49.98	25.00
	κ (mm^{-1})	0.0278	0.0037	0.0040	0.0100

"*" indicates constant parameters in the optimization problem.

optimization step. The optimization problem remains the same as described previously, except that the inner and outer diameters (ID_i and OD_i) of the tubes are set as constants, rather than as optimization variables. The overall design space is therefore reduced to $\mathbf{D} = \{\mathbf{d} \in \mathbb{R}^{3n}, \mathbf{q} \in \mathbb{R}^{2(n-1)\times m\times o}\}$.

The results for both the initial CTR optimization and the intermediate CTR optimization are shown in Table I. The optimized tube set is stable across the entire workspace. Differences in the optimized tube parameters can be seen between the two steps, particularly in the tube curvature (κ). The orientability percentage (Y) is computed post-optimization, where Y is defined as $Y = \frac{r}{o}$, with r representing the number of reachable orientations and o indicating the total number of target orientations. It is important to note that orientation is attained only when the target position is reachable. Here, the specific orientation is considered reachable when the robot tip position error is under 2 mm and the orientation error is less than 10°.

The optimization results for the orientability of both steps are presented in Fig. 4(b), where the orientability percentage of the initial and intermediate optimizations are 78% and 72%, respectively. The body of the robot is restricted to remain in its half of the laryngoscope. As a result, since target 6 and the robot body are located on the same side of the laryngoscope, the majority of orientations can be reached as expected. However, for targets that are at the center or on the other half of the laryngoscope, some orientations cannot be achieved or are difficult to reach due to collisions with the environment. For instance, the robot can reach most orientations when approaching from the right side of target 1, but not from the left side, since it cannot pass through the center line of the laryngoscope, as previously described in Section II-B. Finally, the results illustrate the importance of the two-step optimization process.

B. Uncertainty-Based Selection of Manufacturing Tolerances

In addition to the challenge of matching the optimized tube diameters with those provided by suppliers, a significant source of discrepancy in the design of CTRs arises from the process of shaping the tubes, as described in Section I-B. The difference between the desired tube curvature and the actual curvature after the shaping process can vary and may have a significant impact on the robot's performance. One approach to dealing with these manufacturing discrepancies, has been to measure the true curvature of the physical robot's tubes to ensure the accuracy of the kinematic model for control purpose. However, this approach does not guarantee optimized robot performance, as the tube curvature is no longer the same as the optimized design. Here we propose an alternative approach that allows the user to evaluate the effect of uncertainty in tube curvature on the robot performance and assists the user in determining the fabrication tolerance, as illustrated in the block titled "uncertainty-based selection of manufacturing tolerances" in Fig. 3. The fabrication tolerances are finalized once the user verifies that the tolerances are feasible to achieve and that the robot performance distribution is reasonable.

1) Performance Uncertainty Quantification: In order to understand the impact of fabrication errors on the performance of the CTRs, an uncertainty analysis approach is employed. Previous work on soft growing robots has indicated that the actual geometric specifications likely lie inside a distribution due to manufacturing uncertainty and imprecision, centered around the optimized or target design parameters [24]. In our case, due to spring-back after shape-setting, true curvatures may be lower than the nominal value. To compensate, higher-curvature fixtures are often required, but determining the optimal curvature of the fixtures is non-trivial. As a result, the final curvature of the tube may either be less than or greater than that of the desired value. The uncertainty in the input, specifically the tube curvatures (κ_i), are therefore modeled as Gaussian distributions, $\mathcal{N}(\mu, \sigma^2)$, with mean values equal to the desired curvatures. The standard deviation of the Gaussian distribution for each tube curvature is assumed to be proportional to the curvature. This relationship stems from the understanding that tubes with higher curvatures experience higher internal stress and introduce increased uncertainty due to the spring-back effect. N sets of tube curvatures, $\{\kappa_1, \ldots, \kappa_i\}$, sampled from the distribution of each tube, where $i = 1 \cdots 4$ and $N = 300$, are then propagated through a deterministic model. The joint values, α_i and β_i, are solved to obtain a distribution of the output (Y), which is the CTR's orientability in this case, as shown in the block titled "performance uncertainty quantification" in Fig. 3. This approach provides insight into how the robot's performance is affected by fabrication errors and can inform decisions on fabrication tolerances for the manufacturing process. The distribution for each tube and the results of the uncertainty quantification are shown in Fig. 5(a) and (b), respectively. In order to facilitate the process and lower the cost in manufacturing, this initial uncertainty quantification starts with a relatively high variance for each tube curvature. As a result, as seen in Fig. 5(b), the uncertainty of the output, which is orientability (Y) in this example, results in large variations $\sigma(Y) = 20.40$.

2) Fabrication Tolerance and Performance Uncertainty Check: The tolerance achievable in the fabrication process is highly dependent on the method and equipment used. In order to determine the feasibility of the tolerance, the framework requires engineering knowledge from the designer based on their confidence in the fabrication method. The designer must also evaluate whether the output distribution of their robot performance is acceptable, as shown in the tolerance selection block in Fig. 3. As discussed, the output variance from the initial performance uncertainty quantification is large, and the performance goal cannot be satisfactorily met. In particular, the result of the uncertainty analysis indicates that 30% of the randomly chosen tube sets from the modeled uncertainty will result in low orientability (less than 10%). Furthermore, an examination of the failure mode for low orientability shows that configurations often reach their targets without achieving the desired orientations. This is evidenced by the mean positional accuracy of 60.49%, compared to the mean 46.00% for orientation. Therefore, there is a need to adjust the tube curvature variance in order to satisfy the user expectation and requirement. By reducing the uncertainty of the parameters κ_i, which implies tighter manufacturing tolerances,

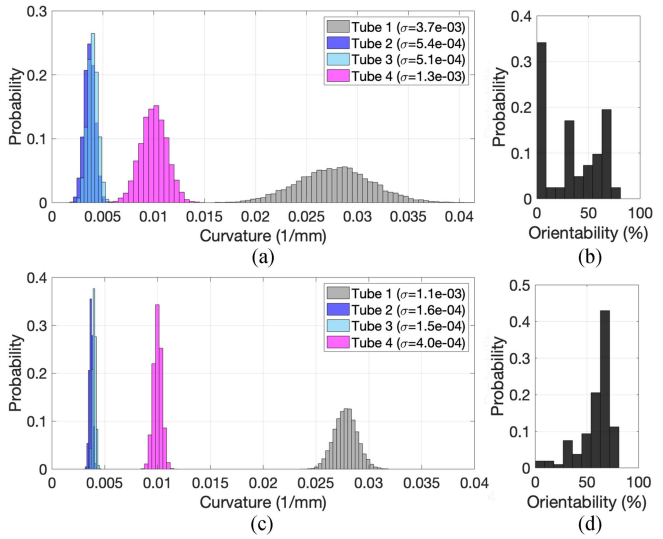

Fig. 5. (a) The initial uncertainty distribution model used for each tube curvature, κ_i. (b) The output result of the first uncertainty analysis that takes into account the uncertainty of tube curvature κ_i. The mean μ and standard deviation σ of the orientability are 46.00 and 20.40, respectively. (c) The final distribution for each tube curvature κ_i. (d) The orientability distribution resulting from the new modeled uncertainty of tube curvature. The mean of the orientability is $\mu = 58.80$ and the standard deviation is $\sigma = 15.90$.

we aim to increase the certainty that the robot achieves the desired orientability for the defined targets.

3) Optimization of Manufacturing Tolerance: In order to determine an appropriate fabrication tolerance that leads to a certain level of robot performance, it is necessary to balance two conflicting factors — manufacturing cost and robot performance. In this study, we assume a reciprocal relationship between fabrication tolerance and cost, which has been proposed for general manufacturing processes, where $\frac{1}{\sigma_i^2} \propto \text{Cost}$ [25], [26]. Specifically, the costs encompass the number of repetitions and the trial and error involved in adjusting fixture curvatures and resistance values, as described in Section I-B. Therefore, the proposed closed-loop design process uses tolerance selection optimization to assist in determining the fabrication tolerance, while ensuring robot performance. To evaluate how changes in each tube curvature (κ_i) affect the orientability (Y), we first note that Y is a discrete variable because we define orientability based on the robot's ability to achieve a finite set of desired orientations. We compute the discrete analogue of the sensitivity of Y with respect to κ — i.e., a difference quotient $\frac{\Delta Y}{\Delta \kappa}$ — and use the corresponding equivalent of the first-order second moment (FOSM) method to approximate $\sigma(Y)^2$ as a linear function of the σ_i^2, where $\sigma(Y)^2 = \sum_{i=1}^{n} \frac{\Delta Y_i}{\Delta \kappa_i} \sigma_i^2$. This approximation of $\sigma(Y)^2$ is then used to formulate an optimization problem that maximizes the fabrication tolerance in order to ultimately minimize the manufacturing costs. The step size is determined through numerical studies to ensure convergence. A linear constraint is imposed as the total cost, d, is a linear combination of all individual input variances with weights w_i, which can be adjusted based on the cost of each tube. Finally, the

Algorithm 1: CTR Design Workflow.

Inputs:
$\mathbf{\Gamma}$: Anatomical model
$\mathbf{S}_t$: Surgical target
$\mathbf{d}_{init}$: Initial robot design
$\mathbf{B}_{init}$: Initial robot base frame
Outputs:
σ_i: Fabrication tolerance
$\mathbf{d_2}$: Robot design
1: $\mathbf{d}_1 \leftarrow$ InitOpt $(\mathbf{d}_{init}, \mathbf{\Gamma}, \mathbf{S}_t, \mathbf{B}_{init})$
2: $ID_i^*, OD_i^* \leftarrow$ Tube selection
3: $\mathbf{d}_2 \leftarrow$ InterOpt
$(\mathbf{d}_1 \backslash \{ID_i, OD_i\}, ID_i^*, OD_i^*, \mathbf{\Gamma}, \mathbf{S}_t, \mathbf{B}_{init})$
4: $Y \leftarrow$ UQ(κ_i, σ_i)
5: **while** σ_i is not feasible or Y is not acceptable **do**
6: $\sigma_i \leftarrow$ TSO(κ_i, Y)
7: $Y \leftarrow$ UQ(κ_i, σ_i)
8: **end while**
9: **return** σ_i, $\mathbf{d_2}$

manufacturing tolerance optimization problem can be described as:

$$\text{Max. } \frac{1}{2}\sum_{i=1}^{n}\frac{\Delta Y_i}{\Delta \kappa_i}\sigma_i^2$$
$$wrt.\ \sigma_i$$
$$\text{st. } d = \sum_{i=1}^{n} w_i \sigma_i, \tag{7}$$

where, Y is the output orientability and σ_i is the optimization variable, which is the standard deviation of the curvature of tube i. w_i is set to be 1, assuming the cost of each tube and manufacturing process are the same. Note that a closed-form solution exists for this optimization problem.

The outcome of the tolerance selection optimization in Fig. 3 generates a collection of new standard deviations for each tube that adheres to the given constraint. It is noteworthy that the total cost d can either be directly determined by the user or can be progressively reduced through an automated continuation approach until the user is content with the outcome. In this study, the latter approach is adopted. The uncertainty quantification block in Fig. 3 is executed again after the optimization of manufacturing tolerance block to evaluate the modified input (tube curvature) and the corresponding output (orientability) distributions based on the newly optimized σ_i. Therefore, these two approaches iteratively optimize the fabrication tolerance until the recommended tolerance is feasible and the output distribution is acceptable, as demonstrated in Algorithm 1.

Using the initial outcomes from the orientability uncertainty quantification displayed in Fig. 5, the closed-loop design process is iterated until the fabrication tolerance is determined. The optimization of manufacturing tolerance highlights that in order to attain a reasonable output probability distribution, all input variances must be reduced, with tube 4 and tube 1 necessitating the most stringent adjustments in this case, as visible in Fig. 5(c).

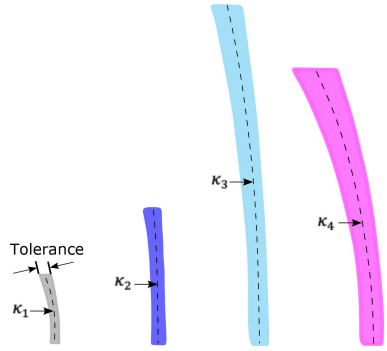

(a)

Tolerance	Tube 1	Tube 2	Tube 3	Tube 4
Max (mm^{-1})	0.0326	0.0044	0.0048	0.0118
Min (mm^{-1})	0.0230	0.0030	0.0031	0.0083

(b)

Fig. 6. The final fabrication tolerance for each tube is presented. The visualization shows (a) the range of curvatures for each tube and (b) the values for the tolerances (maximum and minimum values).

This is mainly due to the outermost tube's significant impact on the workspace location, and the innermost tube's high curvature leading to substantial variance upon initialization, thereby exerting the greatest influence on orientability. The tolerance selection block is then reassessed. Following the design loop's outcomes, the fabrication tolerance is confirmed to be attainable, and the orientability distribution ($\sigma(Y) = 15.90$) is reasonable. The approximation error of the FOSM method is also evaluated, resulting in a discrepancy of 13.6% when compared to the Monte Carlo method. The final lower and upper bounds of the fabrication tolerances, shown in Fig. 6, are determined using $\mu_i \pm 4\sigma_i$, where μ_i equals to the desired tube curvature.

IV. Hardware and System Design

The design and fabrication of the dual-CTR system are presented in this section. We detail the shape setting process used to fabricate the tubes, as well as the design and control of the actuation system.

A. Tube Manufacturing

1) Shape-Setting Process: A modified version of the Joule heat setting approach as described in [12] was used to rapidly prototype the component tubes of the robot. This method enables low-cost and fast prototyping of pre-curved, superelastic Nitinol wires and tubes. The method uses Joule heating to raise the temperature of the material to the required shape-setting temperatures (typically between 500°C and 550°C). The change in electrical resistance is monitored using the relative electrical resistance ratio $R(T)/R_0$, where R_0 is the room temperature electrical resistance and $R(T)$ is the resistance at temperature T, as an indirect means of temperature measurement feedback to control the heating process. Compared to the algorithm used in [12], the tubes are exposed to the heat more gradually. Specifically, the target resistance is increased as a ramp that reaches its

TABLE II
SHAPE-SETTING PARAMETERS AND REPETITIONS OF CTR 2

Tube	Repetition number	Target curvature (mm^{-1})	Fixture curvature (mm^{-1})	Target relative resistance (Ohm)
1	1	0.0278	0.0292	1.19
2	1	0.0040	0.0045	1.19
2	2	0.0040	0.0049	1.19
3	1	0.0038	0.0045	1.19
3	2	0.0038	0.0045	1.20
3	3	0.0038	0.0050	1.20
4	1	0.0100	0.0110	1.20
4	2	0.0100	0.0110	1.20

peak value after 3 minutes and is then held at the peak resistance for 2 minutes to promote a homogeneous distribution of the heat throughout the length of the tubes.

Individual fixtures were 3D printed for each tube using an SLA 3D printer (Photon M3, Anycubic, Hong Kong) with standard 405 nm UV wavelength resin. It was observed that the resin-based 3D printed fixtures maintained their integrity throughout the process of shape setting. Indeed, heat-related damage to the fixtures, which is one source of inaccuracy in the parts, was observed to be less severe than with the medium-density fiberboard fixtures that were used in [12]. The additional precision afforded by the improved heat resistance further improves the reliability and shape accuracy of the method. The details of the fixture curvatures and the number of times that each tube underwent the shape-setting process are provided in Table II. It can be seen that the fixtures were designed with higher curvature than the final desired curvature for each tube in order to compensate for the spring-back phenomenon. While the shape-setting process is repeatable, some factors such as heat transfer away from the tube into the surrounding air and the fixture are not controlled. Therefore, for each tube, repetitions are conducted by increasing the fixture curvature and/or increasing the relative resistance ratio based on a visual inspection (coloration and curvature) after each shape setting attempt. Lack of coloration indicates that proper temperatures are not reached, while an appropriate coloration (typically amber or light purple) but lack of sufficient curvature indicates that an incremental increase in the fixture curvature is necessary.

2) Shape-Setting Results: A target relative resistance value of 1.19 was used to shape set tube 1 (the tube with the smallest diameter) with only one repetition with a 4.86% higher fixture curvature than the nominal target shape. Tube 2 was shaped using a 1.19 target relative resistance value and underwent two repetitions: the first with 13.65% and the second with 21.95% higher fixture curvature values than the nominal target shape. Tube 3 was first shape set at 1.19 target relative resistance value with a fixture curvature of 18.05% higher value than the nominal target shape. It was determined based on the coloration of the tube and the shape of the tube after the attempt that neither the target resistance value nor the chosen curvature of the fixture was high enough for the tube to be shape set properly and within the desired constraints. Hence, the next two repetitions were performed at 1.20 target values, one with 18.05% and one with 30.98% higher curvature values.

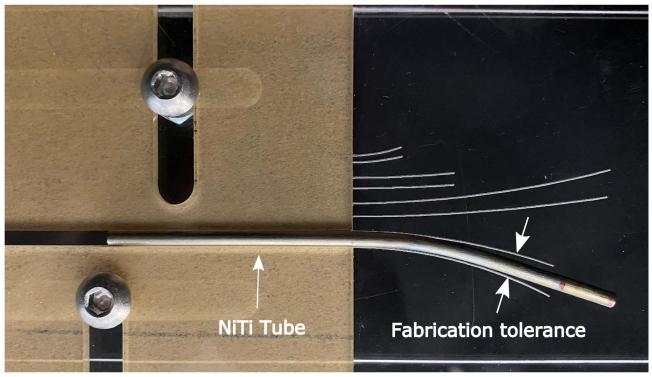

Fig. 7. The fabricated NiTi tube is placed on the tolerance checking tool to assess whether the tube curvature falls within the specified tolerance.

Tube 4 (the largest tube) exhibited the most spring-back and the highest change in the desired material properties and superelasticity. For this tube, it was observed that a target value greater than 1.20 would result in substantial changes to the mechanical properties of the material, including a loss of the quality of the superelastic material properties. However, any target resistance value lower than 1.19 would not result in the necessary temperature rise of the tube and therefore would not result in proper shape setting. Hence a target value of 1.20 was chosen, and the tube was shaped twice with a fixture curvature 10.01% higher than the desired value. To improve the mechanical properties after shape setting, the tube was thermally aged by placing it on a constant temperature hot plate set at 420°C for five repetitions of 1 min 30 s each of heating followed by a quench in room-temperature water. This process did not significantly alter the shape of the tube, as confirmed by visual inspection. The superelasticity was improved by the additional heat treatment, as confirmed by manual manipulation of the tube. Available evidence in the literature suggests that the possible changes in elastic modulus are less significant than the likely changes in plateau stresses. For further information about the effects of aging time and temperature on Nitinol alloys, the reader is referred to [27], [28]. In addition, the mechanical properties are generally believed to have a relatively minor impact in determining the accuracy of the CTR model compared to the shape. In particular, given the fourth power relationship for the area moment of inertia that is involved in bending, the shape is determined largely by the shape of the outermost tube. Therefore, we prioritize the investigation of the uncertainty associated with tube curvature in this work.

We offer two possible explanations for the required differences in shape-setting methods between tubes 1-3 and tube 4. First, it is possible that the tubes had minor or major variations in material composition or thermomechanical history prior to the shape-setting process. Second, some variations are possible due to the fact that the boundary conditions for heat transfer between the tube, the surrounding air, and the fixture change as the diameter of the tube changes. Nevertheless, all tubes were successfully set to a shape within the bounds of acceptable limits, as determined using the tolerance checking tool shown in Fig. 7. The tolerance checking tool consists of a

TABLE III
MEASUREMENT OF TUBE CURVATURE κ (MM^{-1}) FOR EACH ROBOT AND THEIR DISTANCES TO THE MEAN VALUE

	Tube 1	Tube 2	Tube 3	Tube 4
CTR 1	0.0265 ($1.18\sigma_1$)	0.0034 ($1.88\sigma_2$)	0.0035 ($3.30\sigma_3$)	0.0101 ($0.25\sigma_4$)
CTR 2	0.0248 ($2.81\sigma_1$)	0.0039 ($1.25\sigma_2$)	0.0038 ($1.33\sigma_3$)	0.0095 ($1.25\sigma_4$)

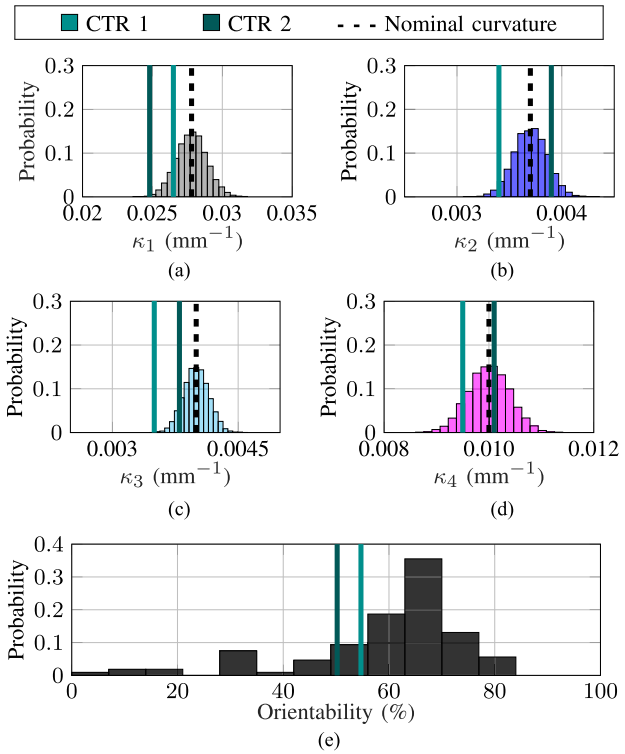

Fig. 8. (a) – (d) The Gaussian distribution of tube curvature for tubes 1 to 4 are shown, along with the measured curvature of the tubes of each CTR. The measured curvatures all fall within the specified tolerance. (e) The orientability of both CTR 1 and 2 lie within the performance distribution, with a distance of 1.08σ and 1.37σ to the mean orientability value.

base plate engraved with the curvature tolerance bounds (upper and lower) for each tube (as shown in Fig. 6(b) using a laser cutting machine. Additionally, it includes two acrylic plates and two screws and nuts to ensure accurate alignment of the tube. The actual tube curvature for each robot is measured and compared to the nominal curvature, with the distance quantified using the metric σ_i, and all values are listed in Table III. To better understand where the true curvature value falls within the fabrication tolerance, the measured curvature values for each tube of both robots are illustrated in Fig. 8(a) to (d), showing their positions within the uncertainty distribution. These results show that the curvature values can be either lower or higher than the mean value, validating our assumption of using both sides of the Gaussian distribution to model curvature uncertainty.

B. Actuation System

A modified version of the actuation system reported in [29] is used. The actuation unit uses a set of nested roller gear mechanisms, where each roller gear can be translated and rotated

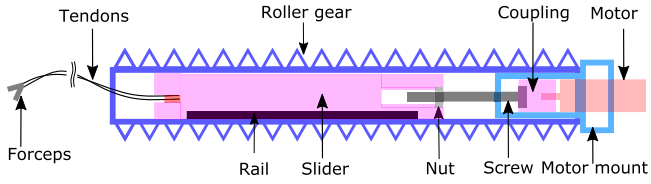

Fig. 9. Schematic showing the miniature end-effector actuation unit that is integrated inside the innermost roller gear. The tendons are connected to the forceps through the innermost tube.

using two spur gears, oriented orthogonally with respect to each other. Each spur gear is driven by a micro gear-motor (Pololu, 1000:1 Micro Metal Gearmotor) with a magnetic encoder (Pololu, magnetic encoder kit 12 CPR). Compared to the system in [29], parameters including the pressure angle of the roller gears and spur gears, along with the length and width of the actuation unit, are modified in order to accommodate the higher friction between the tubes and the design requirements in this particular application. In addition, the fourth tube, referred to as the "tube guide", is rigidly attached to the insertion point and is not connected to the roller gears. The dual-CTR system uses two identical actuation units placed in a Y-shaped configuration, with each unit facing inward towards the other, as discussed in Section II-A1.

A miniature end-effector and associated actuation system were also integrated into the CTR actuation system in order to enable a simulated surgical task. Two off-the-shelf disposable biopsy forceps (OLYMPUS, EndoJaw FB-231D) were selected as end-effectors for this task. The two flexible tendons used to control the opening and closing motion of the forceps were extracted from the outer sheath. The forceps were attached to the distal ends of the innermost tubes of both arms using a heat-shrink tube, and the tendons were then passed through these tubes and into the innermost roller gear, where they were attached to a miniature linear screw system (Fig. 9). We designed this actuation system to be compact in order to fit inside the innermost roller gear (7 mm inner diameter). We also integrated a rail to enable translation and prevent any rotation of the slider to which the tendons are attached. A 6 mm micro DC gearmotor (Pololu, 700:1 plastic planetary gearmotor) was installed within the roller gear, and a coupling component connects the motor shaft and the screw. A nut was rigidly attached on one side of the slider and the other side of the slider was then attached to the back-end of the tendons. Pushing and pulling of the tendons results in the opening and closing of the forceps.

C. Teleoperation Scheme

Two 6 DOF input devices (Phantom Omni, 3D Sysyems) were used to enable the user to teleoperate the two CTRs by controlling the position and orientation of each robot tip. The pose of the stylus of each input device maps directly to each of the robot tip frames. The real-time controller is identical for each CTR and uses the Fourier approximated inverse kinematics proposed in [22]. The Fourier series of order 1 for each joint in $\mathbf{q} \in \mathbb{R}^6$ is used and results in 729 Fourier coefficients for a 6 DOF CTR. The Fourier approximated solutions have average position errors 0.11 mm and 0.51 °. The analytical Jacobian

can be derived directly from the Fourier approximated function. The Newton-Raphson root finding with damped-least squared method is implemented to solve for the joint values given the desired tip frame from the input device and is described as follows [30]:

$$\mathbf{q}_{i+1} = \mathbf{q}_i + \mathbf{J}(\mathbf{J}^T\mathbf{J} + \mathbf{D}(\boldsymbol{\lambda})^2)^{-1}\tilde{\mathbf{g}}, \tag{8}$$

where $\mathbf{q}$ is the joint position, $\mathbf{J}$ is the analytical Jacobian, and $\mathbf{D}$ is the diagonal weight matrix to avoid the joint limits. The joint weight $\boldsymbol{\lambda}$, which depends on the deviation of the joint position q_i from the mean value $q_{i,\text{mean}}$, is described as $\boldsymbol{\lambda} = c(\frac{\mathbf{q}_i - \mathbf{q}_{i,mean}}{\mathbf{q}_{i,max} - \mathbf{q}_{i,min}})^p$, where c and p are the tuning parameters and p is an even number. $\tilde{\mathbf{g}} = \mathbf{g} - \mathbf{g}_{des}$ describes the current tip frame and the desired tip frame [22].

A low-level PID controller is employed to track the reference motor position, which is determined using the desired joint values computed through the inverse kinematics algorithm. Then, the PC sends the command through RS232 serial communication to the motor controllers (Faulhaber MCDC 3006 S RS) at an average rate of 33 Hz. The input device operates at a rate of 1 kHz. Additionally, the push-button on the stylus is used to control the motion scaling factor in the z-direction, which can require adjustment when extracting tissue due to the larger range of motion required. The opening and closing of the end-effector was controlled through two push buttons that are directly connected to a microcontroller (ATmega328P).

V. Experiments and Results

In this section, we conduct hardware experiments in order to compare the performance of the physical robots to the simulation. We also demonstrate the feasibility of the system for use in a micro-laryngeal surgical task.

A. Performance Evaluation

The main goal of using the design workflow and uncertainty analysis is to ensure that the physical robot can achieve the desired performance, which in this case, is orientability. The goal of this experiment is therefore to evaluate the ability of the optimized robot design to reach the six pre-defined target points and orientations identified in Section II-B. We note that although the output of the design optimization also includes a motion plan, these values are not considered here, and closed-loop control is instead used to guide the CTR to reach the target configurations. A 6-DOF Aurora (NDI, Waterloo, Canada) electromagnetic sensor (9 mm length) is attached to the distal end of the robot and the field generator is placed to keep track of the pose of the robot tip, as shown in Fig. 10. In addition, an EM probe and protractor are also used for the calibration of the robot base frame and laryngoscope in order to match the environment geometry in the optimization problem. The recorded robot tip poses are used to evaluate the orientability. Robot configurations are deemed reachable if the tip position is within 2 mm to the target, and the orientation error is less than 10°, as previously discussed in Section III-A. CTR 1 and CTR 2 represent two distinct tube sets, both evaluated using the same actuation unit and on the same side of laryngoscope, due to the symmetric configuration described in Section II-B.

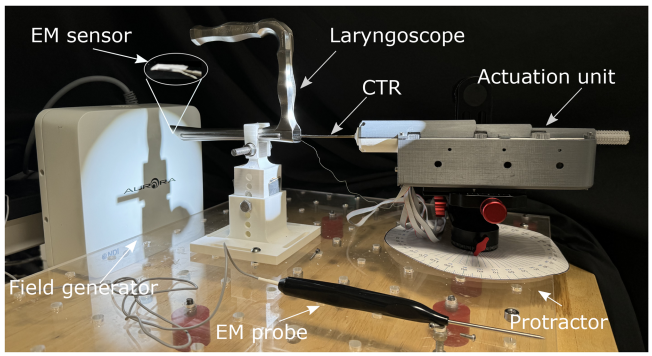

Fig. 10. The experimental setup for orientability evaluation includes a single CTR system with a field generator and an EM sensor attached to the tip of the CTR. The protractor and EM probe are used for calibrating the robot's base frame.

Each tube set underwent three evaluations with different initial home positions, and the average orientability for CTR 1 and CTR 2 was 54.7% and 50.2%, respectively. The results are presented in Fig. 11. The data illustrates that most orientations around 77.5° are attainable by both the physical robots and the optimization results, aligning with the general trend in simulation. However, achieving an orientation of 45° at all the targets is less feasible for the physical robots, possibly due to the tubes having generally lower curvature than the optimized values because of spring-back effects or due to tube clearance. Furthermore, the results indicate that the orientability of the physical robots falls within the distribution outlined in the uncertainty analysis in Fig. 8(e). It is also worth noting that no snapping occurred during the experiments. Although some tubes are close to the tolerance bound as shown in Table III, both robots were still able to achieve average orientability between $50 - 60\%$. While both robots show similar performance based on the orientability metric, this doesn't imply that the robots can reach similar orientations at each target. The actual orientations reached can differ from one another, as shown in Fig. 11. Specifically, at target 5, both robots can reach two orientations at 45°, but the orientations are different. There are several factors that may have contributed to the physical robots not achieving all of the desired orientations. In particular, it is possible that both position and orientation accuracy are influenced by the root-finding method, EM sensor measurements and calibration. In addition, the impact of tube clearance and friction on tip pose, could have contributed to the differences between the physical and simulated robot performance.

B. Demonstration

The primary objective of the final demonstration is to assess the feasibility of using the proposed dual-CTR system for micro-laryngeal surgery. Within this context, we focus here on conducting biopsies and resections of tumors located in the vocal cord area.

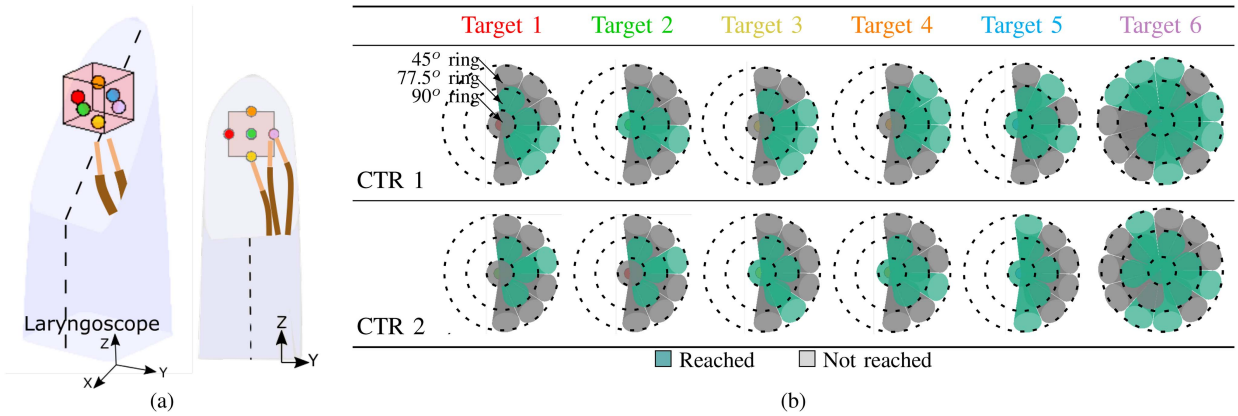

Fig. 11. Orientability results for CTR 1 and CTR 2, collected in a physical experiment. The achievable target orientations are depicted in green, while the unattainable orientations, falling outside the position and orientation tolerances, are shown in gray.

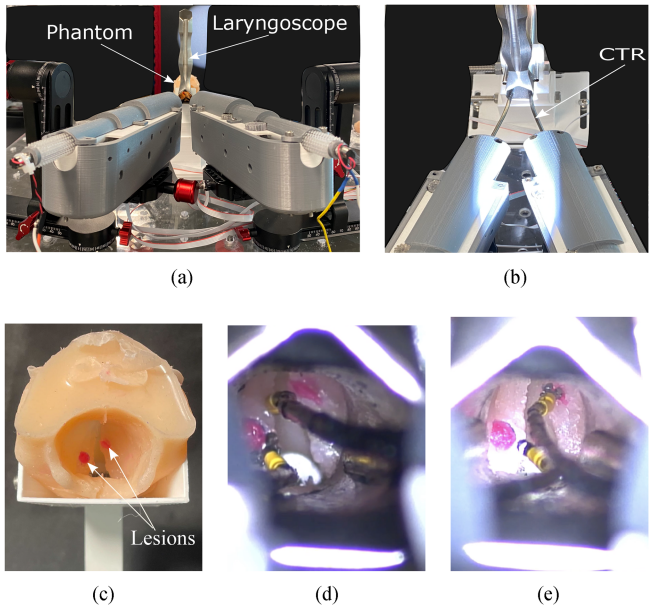

Fig. 12. (a) The fabricated dual-CTR system with the line-of-sight design requirement is shown, along with (b) a close-up view of the CTRs and the entry point of the laryngoscope. (c) The fabricated phantom model is securely mounted on a bracket that is attached to the optical table. Notably, adjustable nodules, highlighted in red, are strategically positioned with two varying sizes and locations to simulate a biopsy task. Screenshots of the biopsy task as observed through the microscope during the user demonstration are shown for the case where (d) the non-dominant hand is used to reach the tumor located on the left vocal fold and (e) the dominant hand is used for the tumor on the top right.

1) Experiment Setup and Phantom Design: The experimental setup consists of two CTR actuation systems, a laryngoscope, and a larynx model, all rigidly mounted to an acrylic optical table as depicted in Fig. 12. The actuation units are connected to a tripod gimbal (Koolehaoda Tripod Gimbal), allowing for easy adjustment of their position and orientation during calibration. Furthermore, the height and orientation of the rigid mount for the laryngoscope and larynx model can be adjusted as well. Additionally, an ENT microscope (Leica F50) is employed to provide visualization to the operator, and the video can be recorded directly for further analysis.

The larynx model is a low-cost, accessible, modular, high-fidelity silicone model. A laryngeal cast was 3D printed with PLA on an Ultimaker. STL files for the cast were based on a previously published open-source design that was created using computed tomography scans of the upper airways processed with 3D Slicer and refined in Blender and Fusion 360, as previously described [31]. This cast was scaled by 1.15x on Ultimaker Cura prior to printing in order to more closely approximate the size of the human glottis based on the experience of several practioning laryngologists. In order to perform silicone injection molding, a Luer lock attachment was created and the inside of the cast was sprayed with silicone releasing agent. The pieces of the cast were then fastened together using glue and adhesive tape. Smooth-On Eco-Flex 20 silicone was mixed as per factory specifications and then injected into the 3D printed cast using a 60 mL Luer lock syringe. After curing for at least 2 hours, the silicone mold was then removed from the cast. In order to simulate a biopsy task, color-dyed silicone nodules of various sizes were then attached to the vocal folds using silicone adhesive.

2) User Test: The two simulated lesions were attached on the right and left vocal folds, as shown in Fig. 12. The placement is to test whether the robot can perform tasks in areas around the workspace boundary shown in Fig. 2, which are challenging to access with a rigid instrument, according to clinicians. The demonstration aims to show the feasibility of using both the dominant and non-dominant hand for the teleoperation of CTRs, with the user instructed to use their left hand for the biopsy of the lesion on the left side and vice versa. A clinician from the Department of Otolaryngology - Head & Neck Surgery at the University of California, San Diego performed the biopsy tasks. Video was recorded through the microscope directly and screenshots of the video are shown in Fig. 12. The biopsy task was successfully completed using the proposed dual-CTR system with both the dominant and non-dominant hand. This demonstration illustrates the feasibility of using the proposed system, workflow, and setup for a biopsy task in micro-laryngeal surgery. In addition, the miniature linear actuation unit was able to provide a sufficient amount of force for grasping and obtaining tissue samples using the biopsy forceps. The designed tube sets also exhibited sufficient stiffness to interact with vocal cord phantom tissue when performing the task. In addition, the CTRs did not experience any snapping motion during teleoperation.

Based on this demonstration, we note several potential directions for future work. First, as is expected given the current control method, the backbone of the two robots can collide during the operation in certain configurations, especially when both of the robots are close to the center of the laryngoscope. Future versions of the system could incorporate control algorithms that explicitly consider or prevent collisions between two robots during teleoperation. Second, the current setup requires precise positioning of the two actuation units and the microscope to maintain a line of sight. A potential option could be to try to eliminate the line-of-sight constraint by integrating a tip camera into the system, rather than relying on direct visualization from the microscope, however, this would require a significant change in the surgical workflow. Third, in order to perform a more diverse set of micro-laryngeal surgical tasks, it becomes critical to develop and integrate other end-effectors. Finally, enhancing the ergonomic setup and designing a more intuitive interface are integral parts of our future work, as we aim to advance towards a user study with several tasks and multiple users.

VI. Conclusion

We have introduced a comprehensive end-to-end design workflow for CTRs that considers manufacturing uncertainties and have demonstrated this framework through a case study on micro-laryngeal surgery. Incorporating manufacturing uncertainties into the design process is particularly important when meeting specific performance requirements is task critical. The significance of closing the loop between designs optimized in simulations and the resulting physical prototypes is not exclusive to CTRs, and our proposed design workflow can be extended to include other types of continuum robots. In addition, the performance metric incorporated into the design optimization can be tailored to align with specific task objectives. In future work, optimization under uncertainty can be seamlessly incorporated into the design optimization framework by modeling the uncertainties associated with the optimization variables (e.g. tube curvature). In addition to incorporating manufacturing uncertainty in the design process, model uncertainty could also be considered to further minimize the gap between simulation and the physical robot.

References

[1] J. Burgner-Kahrs, D. C. Rucker, and H. Choset, "Continuum robots for medical applications: A survey," *IEEE Trans. Robot.*, vol. 31, no. 6, pp. 1261–1280, Dec. 2015.

[2] P. Dupont et al., "Continuum robots for medical interventions," *Proc. IEEE*, vol. 110, no. 7 , pp. 847–870, Jul. 2022.

[3] P. Sears and P. Dupont, "A steerable needle technology using curved concentric tubes," in *2006 IEEE/RSJ Int. Conf. Intell. Robots Syst.*, 2006, pp. 2850–2856.

[4] R. J. Webster, A. M. Okamura, and N. J. Cowan, "Toward active cannulas: Miniature snake-like surgical robots," in *2006 IEEE/RSJ Int. Conf. Intell. Robots Syst.*, 2006, pp. 2857–2863.

[5] J. T. Hwang, "A modular approach to large-scale design optimization of aerospace systems," Ph.D. dissertation, Aerosp. Eng., Univ. Michigan, Ann Arbor, MI, USA, 2015.

[6] J. Burgner, H. B. Gilbert, and R. J. Webster, "On the computational design of concentric tube robots: Incorporating volume-based objectives," in *2013 IEEE Int. Conf. Robot. Automat.*, 2013, pp. 1193–1198.

[7] C. Baykal, L. G. Torres, and R. Alterovitz, "Optimizing design parameters for sets of concentric tube robots using sampling-based motion planning," in *2015 IEEE/RSJ Int. Conf. Intell. Robots Syst.*, 2015, pp. 4381–4387.

[8] K. Leibrandt, L. da Cruz, and C. Bergeles, "Designing robots for reachability and dexterity: Continuum surgical robots as a pretext application," *IEEE Trans. Robot.*, vol. 39, no. 4, pp. 2989–3007, Aug. 2023.

[9] K. M. Lynch and F. C. Park, *Modern Robotics*. Cambridge, U.K.: Cambridge Univ. Press, 2017.

[10] G. Li et al., "An angle–axis space-based orientability index characterizing complete orientations," *IEEE/ASME Trans. Mechatron.*, vol. 27, no. 2, pp. 880–891, Apr. 2022.

[11] I. Nitinol Devices & Components. Nitinol facts. [Online]. Available: https://confluentmedical.com/tech-center/nitinol-university/

[12] H. B. Gilbert and R. J. Webster, "Rapid, reliable shape setting of superelastic nitinol for prototyping robots," *IEEE Robot. Automat. Lett.*, vol. 1, no. 1, pp. 98–105, Jan. 2016.

[13] Z. Dong, "Tolerance synthesis by manufacturing cost modeling and design optimization," in *Advanced Tolerancing Techniques*. Hoboken, NJ, USA: Wiley, 1997, pp. 233–260.

[14] A. T. Hillel et al., "Applications of robotics for laryngeal surgery," *Otolaryngologic Clin. North Amer.*, vol. 41, no. 4, pp. 781–791, 2008.

[15] G. Fiacchini et al., "Is the Da Vinci Xi system a real improvement for oncologic transoral robotic surgery? A systematic review of the literature," *J. Robot. Surg.*, vol. 15, no. 1, pp. 1–12, 2021.

[16] S. Lang et al., "A European multicenter study evaluating the flex robotic system in transoral robotic surgery," *Laryngoscope*, vol. 127, no. 2, pp. 391–395, 2017.

[17] D. T. Friedrich et al., "Teleoperated tubular continuum robots for transoral surgery–feasibility in a porcine Larynx model," *Int. J. Med. Robot. Comput. Assist. Surg.*, vol. 14, no. 5, 2018, Art. no. e1928.

[18] G. Cen et al., "A dual-arm concentric-tube robot system for transnasal surgery," *Procedia Comput. Sci.*, vol. 209, pp. 76–83, 2022.

[19] T. L. Bruns et al., "A modular, multi-arm concentric tube robot system with application to transnasal surgery for orbital tumors," *Int. J. Robot. Res.*, vol. 40, no. 2/3, pp. 521–533, 2021.

[20] J.-T. Lin et al., "A generalized framework for concentric tube robot design using gradient-based optimization," *IEEE Trans. Robot.*, vol. 38, no. 6, pp. 3774–3791, Dec. 2022.

[21] D. C. Rucker et al., "Equilibrium conformations of concentric-tube continuum robots," *Int. J. Robot. Res.*, vol. 29, no. 10, pp. 1263–1280, 2010.

[22] P. E. Dupont et al., "Design and control of concentric-tube robots," *IEEE Trans. Robot.*, vol. 26, no. 2, pp. 209–225, Apr. 2010.

[23] H. B. Gilbert et al., "Elastic stability of concentric tube robots: A stability measure and design test," *IEEE Trans. Robot.*, vol. 32, no. 1, pp. 20–35, Feb. 2016.

[24] J. D. Greer et al., "Robust navigation of a soft growing robot by exploiting contact with the environment," *Int. J. Robot. Res.*, vol. 39, no. 14, pp. 1724–1738, 2020.

[25] A. Armillotta, "Selection of parameters in cost-tolerance functions: Review and approach," *Int. J. Adv. Manuf. Technol.*, vol. 108, no. 1, pp. 167–182, 2020.

[26] M. Sfantsikopoulos, "A cost-tolerance analytical approach for design and manufacturing," *Int. J. Adv. Manuf. Technol.*, vol. 5, pp. 126–134, 1990.

[27] D. Janda, C. Lasley, and T. Duerig, "Limitations on leveraging Af to predict the mechanical response of nitinol," *Shape Memory Superelasticity*, vol. 5, no. 4, pp. 374–382, 2019.

[28] A. R. Pelton, J. Dicello, and S. Miyazaki, "Optimisation of processing and properties of medical grade nitinol wire," *Minimally Invasive Ther. Allied Technol.*, vol. 9, no. 2, pp. 107–118, 2000.

[29] C. Girerd and T. K. Morimoto, "Design and control of a hand-held concentric tube robot for minimally invasive surgery," *IEEE Trans. Robot.*, vol. 37, no. 4, pp. 1022–1038, Aug. 2021.

[30] M. Na, B. Yang, and P. Jia, "Improved damped least squares solution with joint limits, joint weights and comfortable criteria for controlling human-like figures," in *2008 IEEE Conf. Robot., Automat. Mechatron.*, 2008, pp. 1090–1095.

[31] M. Lee et al., "An open-source three-dimensionally printed laryngeal model for injection laryngoplasty training," *Laryngoscope*, vol. 131, no. 3, pp. E890–E895, 2021.